energies

Article

Design and Implementation of a Wireless Charging System Connected to the AC Grid for an E-Bike

Emin Yildiriz [1] and Murat Bayraktar [2,*]

[1] Department of Electrical and Electronics Engineering, Faculty of Engineering, Düzce University, Düzce 81620, Turkey; eminyildiriz@duzce.edu.tr
[2] R&D Department, Farba Automotive, Kocaeli 41420, Turkey
* Correspondence: murat.bayraktar@farba.com.tr; Tel.: +90-262-781-81-18

Abstract: This paper aims to design an IPT for wireless charging of an e-bike and to control the charge of the e-bike from the primary-side. Optimum IPT design has been made according to the 36 V battery bank requirements. The no-load condition test has been performed before charging started in the IPT system connected to the AC grid. The primary-side DC-link voltage of 4–5 V required for this test is provided by the designed forward converter. The charge control has been also made from the forward converter on the primary-side. For this, the forward converter's operation in peak current mode (PCM) has been used. Finally, a prototype has been implemented that works at a maximum DC/DC efficiency of 87.52% in full alignment and 83.63% in 3 cm misalignment. The proposed control algorithm has been tested in this prototype at different load stages.

Keywords: inductive power transfer; wireless charging; e-bikes; forward converter

Citation: Yildiriz, E.; Bayraktar, M. Design and Implementation of a Wireless Charging System Connected to the AC Grid for an E-Bike. *Energies* **2022**, *15*, 4262. https://doi.org/10.3390/en15124262

Academic Editors: Adel El-Shahat and Byoung Kuk Lee

Received: 2 February 2022
Accepted: 4 April 2022
Published: 9 June 2022

1. Introduction

The research about plug-in and contactless charging of e-vehicles is increasing with the increase in the use of e-vehicles all over the world [1]. Depending on the power level and the usage area of e-vehicles, static or dynamic wireless charging can be used. In these power transmission systems, which are loosely coupled due to the height of the vehicle sub-chassis from the ground, the compensation is used on the primary side and secondary side to increase the power transmission efficiency. The main compensation topologies such as Series-Series, Series-Parallel (SP), and also the popular topologies that have additional components such as Inductor/Capacitor/Capacitor (LCC) [2], Inductor/Capacitor/Inductor (LCL) [3,4] etc. have been applied on the primary and secondary sides. The SS topology was preferred in this paper, since it is frequently chosen in the literature at similar power levels and uses fewer components. The other important components in the IPT structure are converter structures. In an IPT system supplied from a 50–60 Hz AC grid, the dual-stage converters are traditionally preferred on the primary side (Figure 1). Particularly in recent years, there have been researchers who prefer the single-stage converter on the primary side [5,6]. By using the matrix converter on the IPT, a more compact primary side is provided independently of the lifetime and cost of the DC link capacitor. However, the dual-stage converter can be designed and controlled independently at each stage and also operates with high efficiency even at variable loads. Thus, this topology has been preferred in many industrial applications [7].

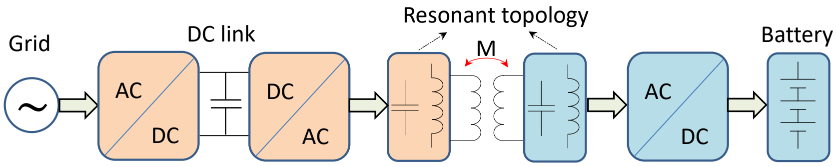

(**a**)

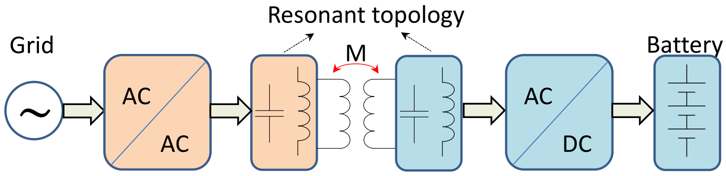

(**b**)

Figure 1. Primary side configurations of IPT: (**a**) Dual-stage; and (**b**) Single-stage.

The battery characteristics should be taken into account when designing an IPT for the electrical device to be wirelessly charged. For the battery to operate in a healthy and long-lasting manner, it must be charged in Constant Current (CC) and Constant Voltage (CV) mode according to the battery charge profile [8]. During the charging process, the equivalent load resistance (R_o) is not constant as the charging current and voltage change. Although the mutual inductance between the coils (M) is constant in the full-alignment state, the transferred power, efficiency, charging current, and voltage also change since R_o changes.

The charging current and voltage can be controlled from the primary side, the secondary side, or both sides in case of misalignment or load changes. If the control is undertaken on the secondary side, the desired control can be achieved with the current and voltage data of the load. The control is achieved with an added DC/DC converter or using a controlled rectifier on the secondary side [9,10]. That is, the control from the secondary side does not require communication components but creates a more complex secondary side. When performing CC/CV control from the primary side, the variation of the load current and voltage must be known or estimated. These data can be transferred from the secondary side to the primary side via a wireless communication link [11,12]. However, the data transmission security may be compromised in cases such as misalignment or the presence of any foreign objects. The parameter estimation approach can be based on the load estimation [13,14] and/or the mutual inductance estimation [15]. The CC/CV control from the primary side is generally based on operating the H-bridge inverter with variable frequency or the phase-shift method [16,17]. The variable frequency operation may affect the power transfer performance and the efficiency due to divergence from the resonance frequency. The phase-shifting method is the most widely used [4,18]. However, the phase-shifting method does not allow the use of a standard soft-switched inverter. Moreover, achieving the secondary side control with the phase-shifting method on the primary side as in the e-bike application focused on in this study (an IPT with a DC-link voltage of 400 V on the primary side and also a low voltage on the secondary side) is very difficult. This is because the change sensitivity of the phase-shift angle must be very high. Therefore, the sensitivity of the phase-shifting limits the secondary side DC link voltage. Consequently, a DC/DC converter is required for the CC/CV control from the primary side of IPT applications, such as the wireless charging developed for the e-bike and sourced from a 230 V AC grid.

Nowadays, the research on wireless charging of e-vehicles is generally focused on a power level of 3.3 kW and above. The primary side and secondary side DC-link voltages are usually 400 V in IPT designs for these power levels [19–22]. Whereas the primary side DC-link voltage is determined according to the AC grid, the secondary side DC voltage is related to the battery bank voltage. The power level to be transferred in the charging of e-bikes and the voltage level of the battery group are low. In e-bike applications encountered in the literature, the system responses have been examined by connecting a DC supply to the inverter input [23–29], or a DC-link voltage in the range of 60–85 V can be achieved on the primary side using a grid-connected step-down transformer [30]. In these papers, the CC/CV control was carried out with the phase-shifting method over the h-bridge inverter. Using a DC/DC converter instead of a step-down transformer at the inverter input provides a more compact primary pad. A dual-stage converter was used in [31], and a buck converter was preferred at the inverter input. Due to the operation limits of the buck converter, this wireless charging system requires the use of a DC/DC converter on the secondary side for the charge control. In this case, both the use of more components has emerged and the idea of a simple secondary side acquisition has been moved away from. Considering the researches on wireless charging of e-bikes that use low secondary side DC-link voltage, the main contributions of this paper are summarized as follows.

(1) A wireless charging system connected to the AC grid has been designed to meet the battery charging requirements of the e-bike.
(2) The IPT and AC grid are isolated from each other by the use of a forward converter. At the same time, the low primary side DC-link voltage required testing the presence of load and large misalignment can be provided with the forward converter.
(3) The CC/CV control is achieved with a forward converter working in PCM mode instead of an H-bridge inverter. Thus, the soft-switching methods can be easily applied in an inverter operating at a constant frequency and duty-ratio.

The organization of this paper is as follows. The optimum IPT design was carried out considering the charging requirements of the e-bike, as described in Section 2. Then, the design of the forward converter, in which the charge control and the no-load condition test were carried out, is presented. The simulation and experimental results are presented in Section 4, comparatively. Finally, Section 5 concludes this paper.

2. Design of Inductive Power Transfer System for E-Bikes

The limits of electrical parameters such as DC-link voltages and resonance frequency, as well as physical criteria such as the air-gap of the power transfer, should be determined correctly when starting an IPT system design. Wireless charging of a 250 W e-bike with 36 V, 20 Ah gel batteries was investigated in this paper. The charging system's input is connected to a 230 V AC grid. The general scheme of the system is given in Figure 2. According to the battery characteristics, the maximum voltage needed to charge the 3 × 12 V battery pack is 44 V. When charging at a constant current, the charging current is required to be 2.5 A.

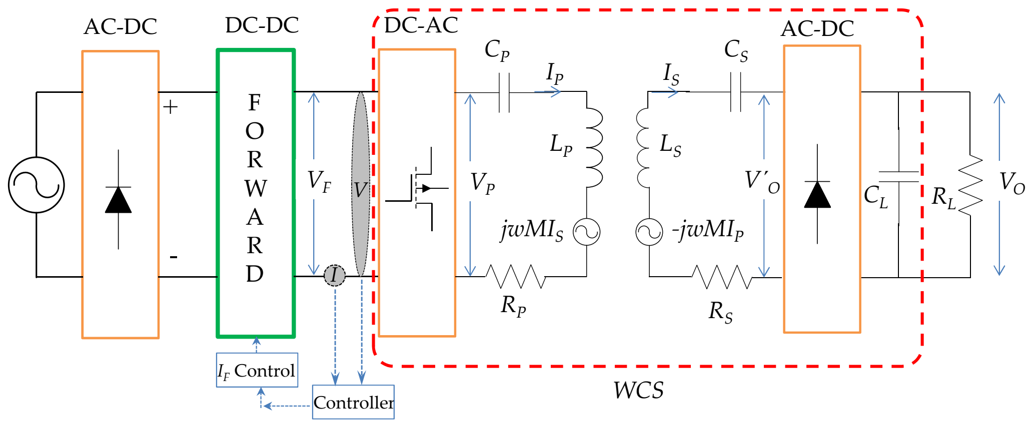

Figure 2. Structural diagram of the IPT proposed for e-bike wireless charging.

The secondary side output voltage of the IPT, V_o' is calculated using Equation (1) according to the battery charge requirements. The primary and secondary side voltages are expected to be close to each other for optimum coil usage [32]. The primary side voltage V_P was selected considering this closeness relation. There is a relationship between the output voltage of the DC-DC converter (V_F) and V_P as in Equation (2). Accordingly, a forward converter was preferred in this study in order to reduce the output voltage of the rectifier connected to the AC grid to the desired DC voltage level.

$$V_o' = \frac{\pi}{2\sqrt{2}} V_o \tag{1}$$

$$V_P = \frac{4}{\pi\sqrt{2}} V_F \tag{2}$$

The voltage equations of the primary and secondary side are written as Equations (3) and (4) for SS topology. Here ω is the resonance frequency. The self-inductances (L_P and L_S) of the primary and secondary side windings depend on the winding dimensions and the number of turns, which are decided according to the coil design. Primary and secondary resonance capacitors (C_P and C_S) are determined considering L_P, L_S, and ω. Another important parameter in voltage equations, R_o, is the equivalent resistance at the rectifier input and is calculated from Equation (5). The primary and secondary sides are expected to operate in resonance during the power transmission. Thus, the efficiency of the power transfer can be calculated from (6). Using Equation (4), the ratio between primary and secondary side currents is written as in (7). Equation (8) is obtained when this ratio is used in Equation (6). Consequently, the change in load and mutual inductance directly affects the power transfer efficiency (PTE).

$$V_P = R_P I_P + j\left(L_P\omega - \frac{1}{C_P\omega}\right) I_P + j\omega M I_S \tag{3}$$

$$j\omega M I_P = R_S I_S + j\left(L_S\omega - \frac{1}{C_S\omega}\right) I_S + R_o I_S \tag{4}$$

$$R_o = \frac{8}{\pi^2} R_L \tag{5}$$

$$PTE = \frac{R_o {I_S}^2}{R_P {I_P}^2 + R_S {I_S}^2 + R_o {I_S}^2} \tag{6}$$

$$\frac{I_P}{I_S} = \frac{R_S + R_o}{\omega M} \tag{7}$$

$$PTE = \frac{R_o}{R_P\left(\frac{I_P}{I_S}\right)^2 + (R_S + R_o)} = \frac{R_o}{R_P\left(\frac{R_S+R_o}{\omega M}\right)^2 + (R_S + R_o)} \tag{8}$$

The resonance frequency and mutual inductance should be high for maximum PTE, as seen in Equation (9). However, as the operating frequency increases, the effective series resistance (ESR) of the coils increases too. Therefore, quality factors should also be taken into account in the PTE calculation. The quality factors of the primary and secondary sides must be carefully selected to avoid bifurcation during charging. The quality factors are calculated as in Equation (10) for the SS topology. Q_P and Q_S values are usually chosen to be close to each other and to be $Q_P > Q_S$ [33,34].

$$\omega M \gg \sqrt{R_P}(R_S + R_O) \tag{9}$$

$$Q_P = \frac{L_P R_O}{\omega M^2},\ Q_S = \frac{w L_S}{R_O} \tag{10}$$

In the optimum IPT design, besides electrical constraints such as input and output voltages and required power, the physical constraints should also be taken into account. The maximum outer dimensions of the coils and power transmission height are known, due to the sub-chassis size limitation. In order to protect the secondary winding fixed to the sub-chassis of the e-bike, a plastic protective cover according to the winding dimensions was prepared. The height of the impact-proof plastic cover was 10 cm from the ground. The maximum area that the secondary winding could use was 240 × 280 mm, considering the sub-chassis limits. In order to make the most of this area, a rectangular winding pair was preferred. In this study, a coil pair with an air core was chosen in order to avoid additional weight on the bicycle. Thus, since the winding inductances can be calculated analytically, not FEA, the optimum winding pair could be determined quickly.

In addition to physical constraints, design constraints such as winding current densities, maximum frequency, and the avoidance of bifurcation should also be considered. It is possible to use smaller winding pairs for the same power transfer as the operating frequency increases. However, the magnetic flux density outside the power transmission region also increases with the operating frequency. The maximum operating frequency of the optimal IPT to be designed was selected at around 85 kHz, considering compliance with ICNIRP and IEEE c95.1 standards and SAE J2954 criteria. The maximum winding current density was determined as 3 A/mm^2 in order to keep the thermal effect small.

The winding designs capable of transmitting the desired power were scanned with an algorithm as in [33], considering the determined design constraints and physical constraints. The self and mutual inductances of the air-core windings were calculated analytically. The winding inductances depend on the winding dimensions and the number of turns. The K_D parameter was used to determine the best winding pair among the winding pairs that could transfer the desired power. The K_D parameter is a design factor, which is determined by the winding quality factors and the maximum operating frequency, and defined as the winding utilization factor [35].

The parameters of the optimum IPT are given in Table 1. The windings were wound with 38 AWG litz wire, taking into account the operating frequency and the current density. When a load close to the equivalent load was connected to the secondary side, the current and voltages close to the design values were measured experimentally. In the experimental study, the winding resistances were high due to the additional connection lengths. This situation was also reflected in the observed experimental efficiency.

Table 1. Design parameters of the optimum IPT.

Parameter	MATLAB	Measured
R_P (Ω)	0.3698	0.433
R_S (Ω)	0.3501	0.4067
L_P (µH)	205.1179	203.1
L_S (µH)	189.9593	187.31
M (µH)	26.4054	25.5
C_P (nF)	17.1281	17.447
C_S (nF)	18.4895	18.791
V_P (Volt)	41.1	41.1
I_P (A)	2.9087	2.94
I_S (A)	2.8465	2.85
f_0 (kHz)	84.9234	85.19
$P_o{}'$ (Watt)	113.5933	113.145
η (%)	95.012	93.18

The load in the designed IPT system is not static. The equivalent resistance value will also change with the battery charge level. The current and voltage gains for different loads were calculated according to the design parameters. Due to the nature of the SS topology, an uncontrolled IPT system operates in CC mode. Since the magnitudes of the current-voltage gain G_{I-V} are small, a limited change in current is observed in the load changes that may occur while operating at the resonance frequency (as seen in Figure 3a). When the voltage gain for load changes is examined, it is seen that G_{V-V} increases significantly as the resistance value increases at 85 kHz, for which the IPT is designed (Figure 3b). In other words, due to the nature of the SS topology, it cannot give a constant voltage output at variable loads. Therefore, especially when the secondary side is open-circuit, the output voltage can reach dangerous points.

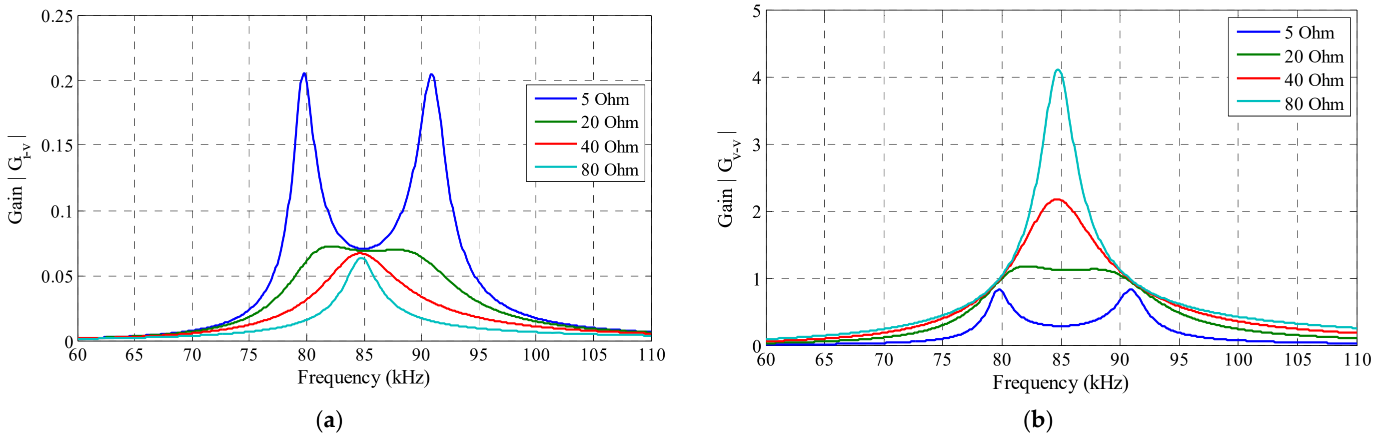

Figure 3. Frequency responses of the designed IPT system: (**a**) G_{I-V}; (**b**) G_{V-V}.

3. Forward Converter Design

The forward converter isolates the input and output sides of the converter from each other using the forward transformer. 300 V DC voltages can be stepped down to 5–10 V using a forward converter. Considering the switching times of the semiconductor circuit elements, it is difficult to obtain such a duty cycle with a buck converter. Although the power levels of forward converters are limited, a forward converter can be used in cases in which the required power is low (44 V × 2.5 A), as in this study.

In the two-switch forward converter, the current and voltage stress that the switches are exposed to is less than that of a single-switch one. The equivalent circuit of the two-switch forward converter according to the ON and OFF operating modes is shown in Figure 4. When the switches (Q1 and Q2) are ON, energy is transferred depending on the conversion ratio from primary to secondary of the transformer. At this moment, D3 is ON, whereas D4 is OFF. When the switches turn off, the primary winding of the transformer is reversely connected to the input voltage via D1 and D2. Thus, there is no need to use an additional winding to reset the transformer. On the secondary side, the voltage of L_F reverses. Therefore, D3 turns off and D4 turns on. Thus, the linearly decreasing current of L_F continues to flow. The output voltage of the forward converter is calculated from Equation (11). Here η_F, N_F, D denote the converter efficiency, forward-turn ratio and duty ratio, respectively. The turn ratio of the transformer is calculated taking into account the maximum of the duty ratio and the minimum input voltage. L_F and C_F are calculated according to the limited current and voltage ripple.

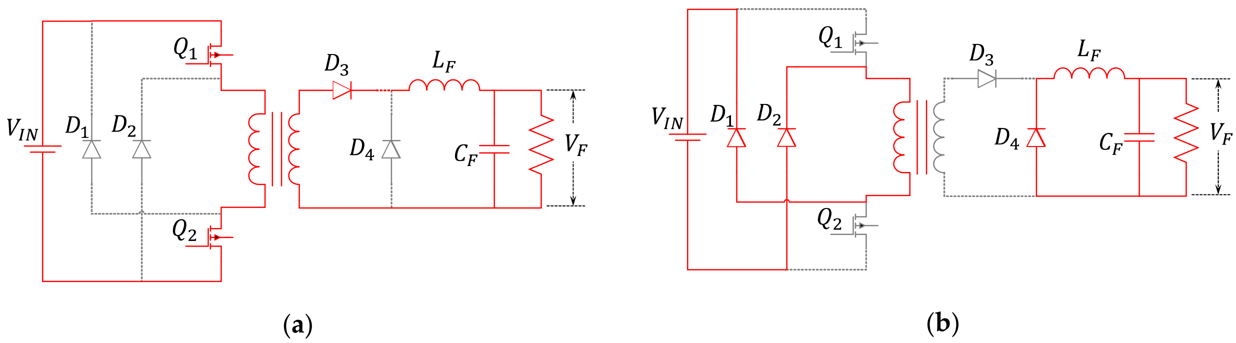

Figure 4. The equivalent circuits of the two-switch forward converter: (**a**) ON state; (**b**) OFF state.

The voltage ripple of the converter output will further increase the voltage ripple in the charging process. Therefore, the magnitude of the capacitor at the converter output is important (12). Here ω_F is the forward switching frequency, and ΔI_F and ΔV_F represent the ripple in current and voltage of the forward converter output, respectively. The input of the forward converter is connected to a single-phase full-wave rectifier. The parameters of the designed forward converter are given in Table 2.

$$V_F = \eta D V_{IN} N_F \tag{11}$$

$$C_F = \frac{\Delta I_F}{\omega_F \Delta V_F} \tag{12}$$

Table 2. The parameters of the forward converter.

ΔI_F	250 mA	D	% 15–47
ΔV_F	10 mV	N_F	1.63
V_{IN}	310 V	η	% 96
C_F	1000 uF	L_F	330 uH

4. The Control Strategy of No-Load Condition and Charging

4.1. No-Load Condition Control

Two separate controls work at the same time in the developed IPT. These are no-load condition control and charge control. Before starting charging, the presence of the load is tested. For this, the duty cycle of switches Q1 and Q2 is set to D_{test} so that the output voltage of the two-switch forward converter is equal to V_{F_test}. At this moment, the current of the forward converter I_F, is measured. If I_F is not less than I_{F_max1}, the system is kept in the load-test section. I_{F_max1} is the limit current value for the primary side's safe operation. If $I_F = I_{F\_max1}$, this could be for two reasons. First, it could be a secondary side open circuit. In the other case, there may be a fully charged battery on the secondary side. In both cases, it is kept as $V_F = V_{F\_test}$. The no-load condition control also works during the charging process. Thus, if the load is disconnected during charging, the primary side is protected. The no-load condition control is shown as Section-I in the control algorithm (Figure 5).

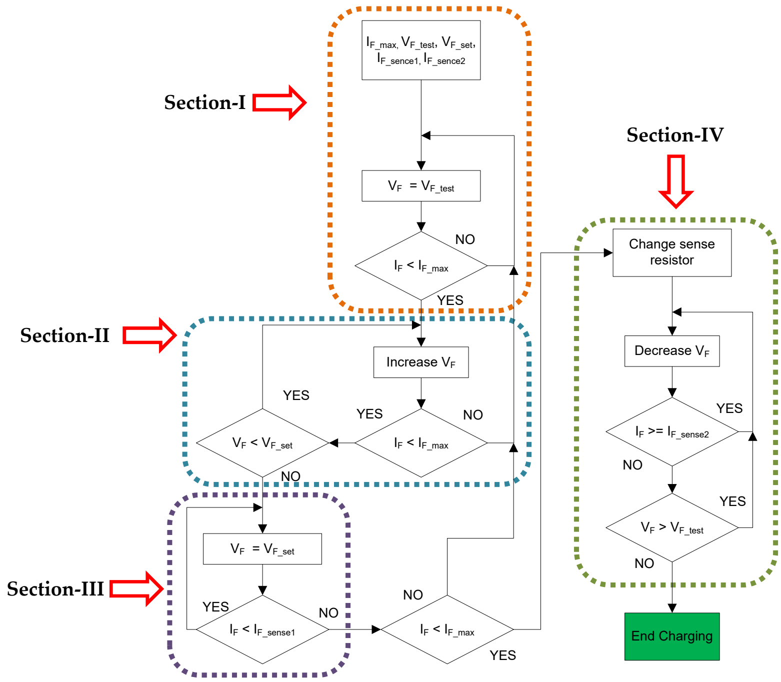

Figure 5. Flow chart of the control algorithm for wireless charging.

4.2. CC-CV Control Strategy

D is gradually increased starting from the D_{test} value, after the no-load condition test is passed. Thus, V_F also increases. In each step, it is checked whether the forward current exceeds the allowable upper limit. The increase in D continues until $V_F = V_{F\_set}$. Thus, $V_{F\_set} = 60$ V value to be applied for charging in constant current mode is reached. This part is shown as Section-II in the control algorithm.

When $V_F = V_{F\_set}$, and I_F has not reached I_{F_sense} yet, the equivalent impedance value of the battery is quite low and charging has started in CC mode. The nature of SS topology tends to keep the secondary side current constant. The secondary side output voltage increases with the increase in state of charge (SOC). At this moment, if it is on the primary side, I_F will increase. The charging process continues in CC mode until the $I_F = I_{F\_sense1}$ condition is met. When $I_F = I_{F\_sense1}$, the charging process has reached the stage of switching to CV mode in CC mode. This part of the control strategy is shown in Figure 5 as Section-III.

In the CV mode of the charging process, the equivalent resistance of the battery bank tends to rise rapidly. The limit current value must be reduced to the second peak current level (I_{F_sense2}) so that I_F current does not quickly reach the maximum value. As the charging process continues, I_F tends to increase. After this point, V_F is reduced to prevent the increase in I_F. For this, D is gradually reduced. At each step, it is checked whether I_F reaches the second peak current value. This loop continues until $V_F = V_{F\_set}$ (Section-IV). If this condition is met, the battery is now full and the charging process is completed.

5. Simulation and Experimental Results

The IPT parameters obtained in Table 1 were used to simulate the whole system on LTspice. The magnetic coupling (k) between L_P and L_S, and the equivalent load, are defined as variables in the simulation model of the whole system. k is determined from Equation (13) for the fully aligned coil pair. In order to accurately model and observe the system response, the open-loop response of the wireless charging system was first examined. Then, the developed controller performance was observed. The load parameter in the simulation was changed at 100 ms, 180 ms, and 240 ms of the simulation, considering the load stages used in the experimental study.

$$k = \frac{M}{\sqrt{L_P L_S}} \tag{13}$$

The experimental studies were carried out on a multi-stage and programmable load group to observe the response of the controller algorithm since the charging time of the batteries took a long time. Figure 6 shows this load group and the designed IPT system in full alignment. Experimental measurements were made at the 100 mm distance using the fully aligned coil pair.

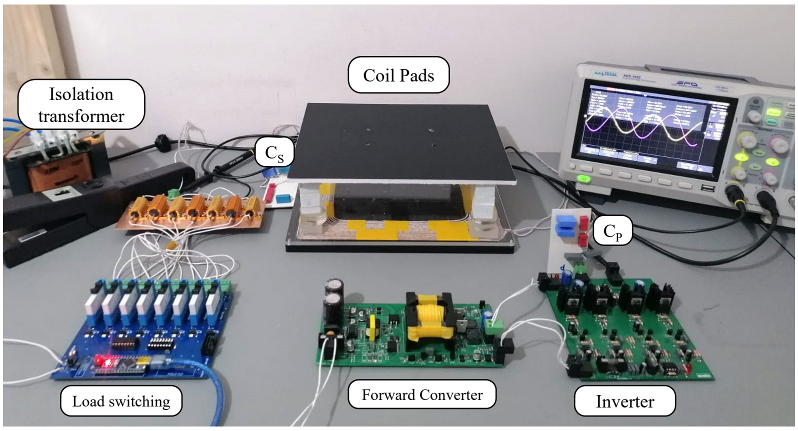

Figure 6. Experimental setup of the primary-side controlled IPT.

5.1. Open Loop System Response

While switching from CC mode to CV mode, V_o voltage is 44 V and I_o current is 2.5 A. At this point, the R_L equivalent battery resistance is 17.6 Ω. The IPT system must operate in CC mode below the equivalent load, and in CV mode above it. The R_L magnitudes to be used in the simulation were selected by considering the nominal values of the resistors used in the experimental study. Accordingly, R_L was set to 8.5 Ω, 10.5 Ω, and 14 Ω, respectively, to examine the CC mode. In this mode, V_F was kept constant at 60 V.

According to the experimental results, as the equivalent resistance increases, the load voltage V_o also increases (Figure 7a). The load current I_o is not affected by the load change as a general response of the SS topology (Figure 7b). V_o and I_o seen in the simulation results also coincide with the experimental results (Figure 7c,d).

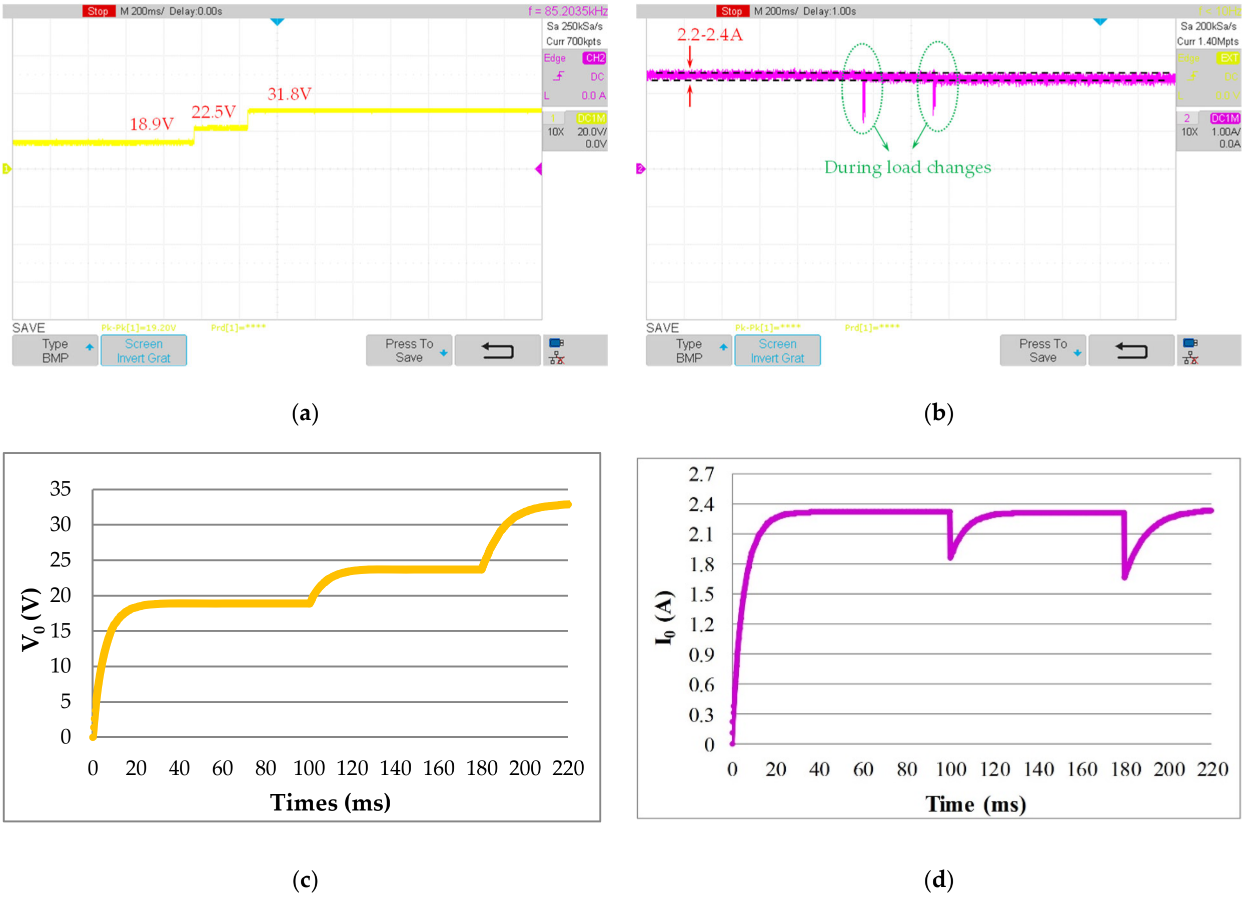

Figure 7. (**a**) measured V_O; (**b**) measured I_O; (**c**) simulated V_O; (**d**) simulated I_O when R_L is 8.5 Ω, 10.5 Ω, and 14 Ω, respectively.

The range of the R_L change is 17.6–440 Ω in CV mode. As SOC increases, the equivalent R_L will also increase too. In this case, the load power increases with the increasing output voltage. Therefore, the primary side current I_P will increase. The forward voltage was set to 40 V in this section of the experiment in order to protect the circuit elements. The load was increased from 16 Ω to 22 Ω, 28 Ω, and 32 Ω for the test in the CV section. As seen in Figure 8a, V_o continues to increase. For R_Ls in the CV section, the simulation model gives close responses to the experimental results (Figure 8b). If the variation of I_P is examined depending on R_L, it is seen that the primary side current magnitude doubles its nominal value at 32 Ω, although a V_F is applied below the nominal operating voltage (Figure 8c). Considering that the equivalent resistance value will approach 440 Ω when the battery is fully charged, it is obvious that the primary side current must be controlled.

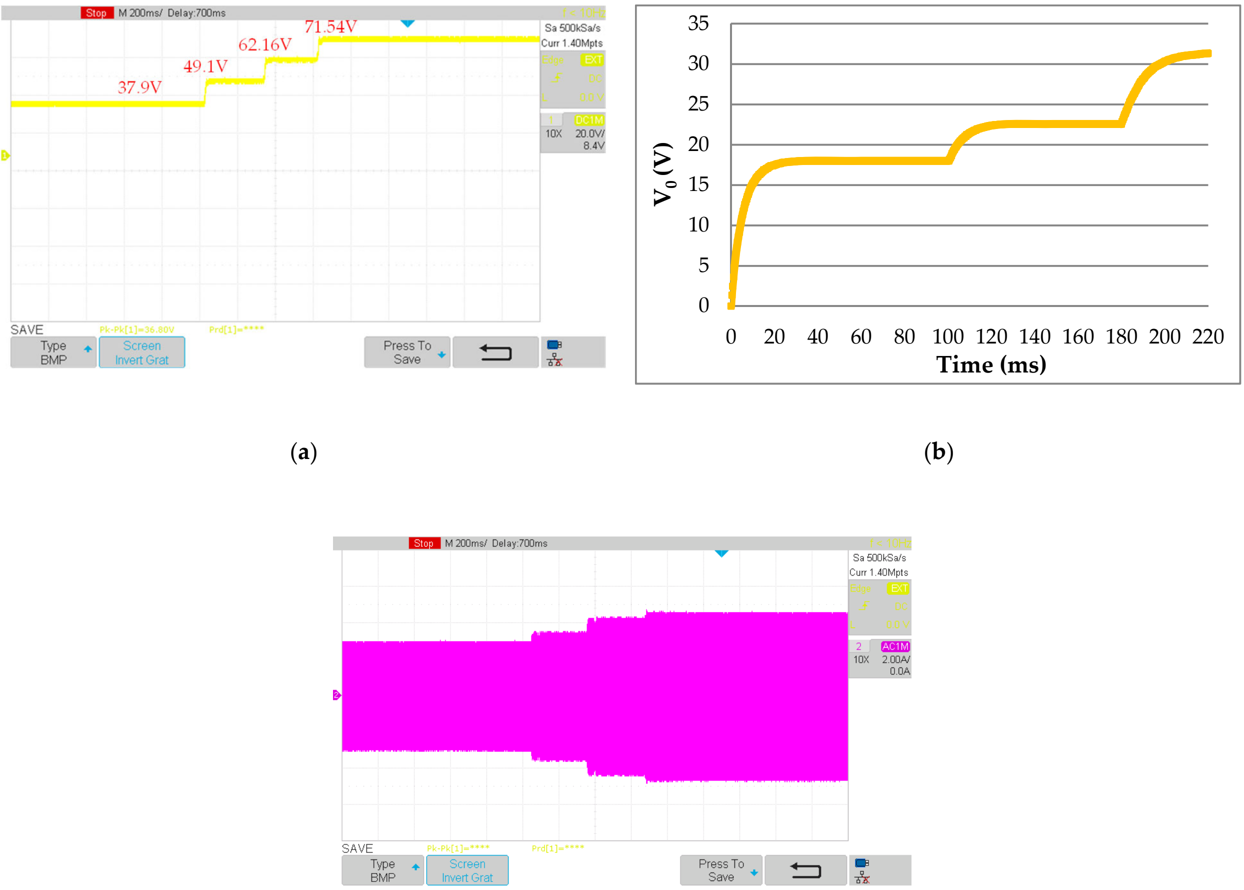

(**a**) (**b**)

(**c**)

Figure 8. (**a**) measured V_O; (**b**) simulated V_O; (**c**) measured I_P when R_L is 16 Ω, 22 Ω, 28 Ω, and 32 Ω, respectively.

5.2. Closed Loop System Response

Switched load magnitudes were selected as 12.8 Ω, 17 Ω, 22.6 Ω, and 32 Ω to observe the overall system response in CC and CV modes. The output voltage of the forward converter was fixed at 60 V for the system that passed the test section of the algorithm (Figure 9a). It was shown before in Figure 7b that I_o did not change due to the SS topology effect in resistance changes up to 14 Ω. Therefore, a single resistance level of 12.8 Ω was considered sufficient to show the charge in CC mode in this section. The charging took place in CC mode in the first part of the control algorithm.

When the resistance increases from 12.8 Ω to 17 Ω, the output voltage V_O increases (Figure 9b). In this case, since the forward current will tend to increase rapidly, the voltage V_F is decreased by the control algorithm. However, a slight decrease was observed in I_O. While the resistance is 22.6 Ω, the charge continues in the CV section. I_O decreases with the increase in SOC (Figure 9c). The output voltage was kept constant by reducing V_F. When the resistance was increased from 22.6 Ω to 32 Ω, V_O was kept constant, and the I_O charging current continued to be decreased. If the resistance magnitude continued to increase at this stage of the charge, it would continue to be throttled until V_F was equal to V_{F_test}.

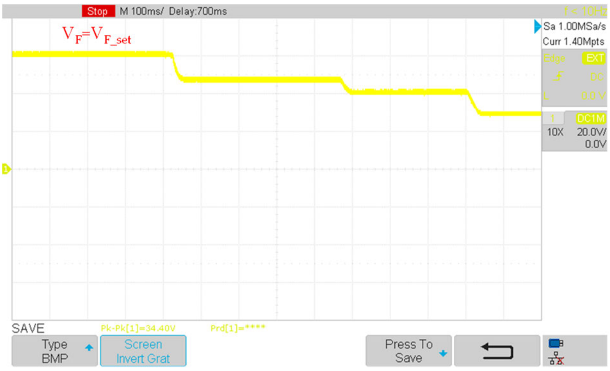

(**a**)

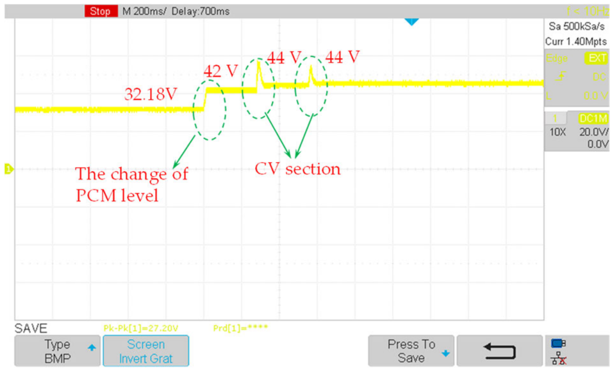

(**b**)

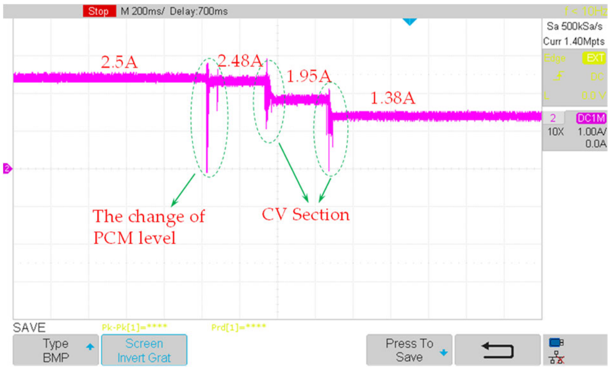

(**c**)

Figure 9. Experimental results of the control algorithm: the change of (**a**) V_F; (**b**) V_O; (**c**) I_O.

In the experimental results, there is an overshoot in the V_o waveform and an oscillation in the I_o waveform due to the sudden change in the load level. In the actual battery charge, these fluctuations will not be in question since there is not be such a sudden change in the equivalent resistance of the battery according to the SOC. In fact, these sudden changes can in practice be caused by a sudden change in the mutual inductance due to the occurrence of misalignment during charging or an object entering between the coil pads. These situations can be identified by detecting high-amplitude inrush current changes.

The primary side should be protected by reducing the forward converter output voltage, if the secondary side is open-circuit at any stage of the charge. The load resistance was increased from 30 Ohm to 440 Ohm for observing this situation in the LTspice model. The variation of V_F with the change of the resistance in the forward converter is shown in Figure 10. The V_F voltage is reduced to 4.041 V. At this moment, I_F also reaches the maximum allowable value. The variation of the current passing through the inductance L_F in the forward converter with the switching of the load is shown in Figure 10b.

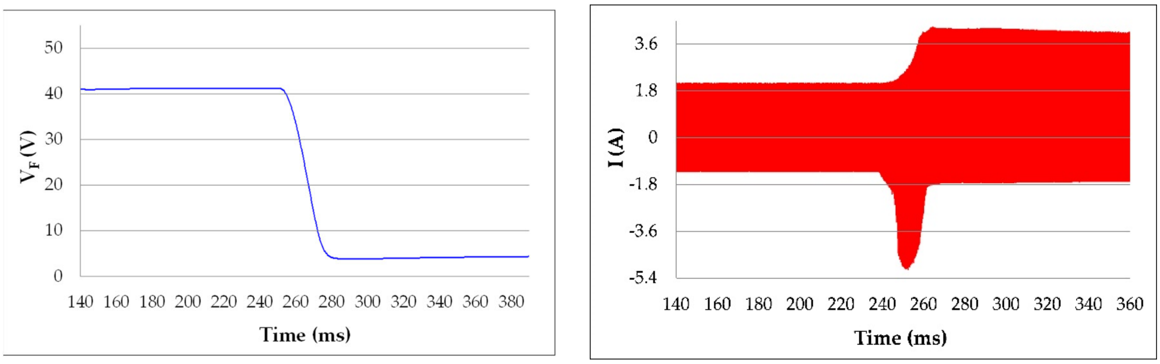

(**a**) (**b**)

Figure 10. (**a**) V_F; (**b**) the current of L_F when disconnecting from the load.

The wireless charging system for the e-bike developed in this paper was compared with the same power level IPTs in terms of efficiency. As can be seen in Table 3, the IPT proposed in this study provides the desired power transmission with higher efficiency at a higher transmission distance than its counterparts. Moreover, since the DC-link voltage on the primary side is high, it can be directly connected to the AC grid.

Table 3. The comparison of WCSs of similar power level.

	Topology	Primary Side Voltage (V)	Secondary Side Voltage (V)	Power (W)	Distance (mm)	Freqency	Eff. (%)
[3]	LCL-LCL	50	50	100	180	1 Mhz	73.6
[17]	S-S	48	18	53,79	30	85.5 kHz	81
[18]	LCL-S	48	26	78,31	35	85 kHz	84.103
[23]	S-S	20	20	90	-	95.6 kHz	90.3
[25]	S-S	-	24	100	30	-	79
[26]	S-S	24	48	250	200	200 kHz	92.15
[27]	S-S	72	48	100	30	100 kHz	-
[29]	S-S	48	36	-	30	100 kHz	-
[29]	S-LCC	48	20	55	-	200 kHz	-
[30]	S-S	~21 V	44,5	84	-	85 kHz	93.17
[31]	S-S	400 V	42 V	100	70	83.1 kHz	80
Prop.	S-S	310 V	44 V	110	100	85 kHz	87.52

6. Conclusions

A wireless charging system, which uses a dual-stage configuration and is supplied from a 230 V AC grid, was designed for charging the 36 V battery bank of an e-bike in this study. An optimum IPT for wireless charging was developed using the dimensions and components obtained in the analytical design. Developed in the SS resonance topology, the current on the primary side of the IPT can reach dangerous values if the charge is in CV mode, the secondary side is open circuit, or in the condition of large misalignment. A forward converter operating in PCM mode limits the current on the primary side. The response of the forward converter was simulated by open- and closed-loop control with LTspice and experimentally verified. Accordingly, the experimental efficiency of the whole system was calculated for full alignment and 3 cm misalignment. The maximum WCS efficiency was 87.52% in the perfectly aligned condition, whereas the maximum efficiency in the 3 cm misalignment was 83.63%. According to the simulation results, these efficiencies are 90.45% and 87.81%, respectively. In addition, the response of the control algorithm was experimentally validated in open-circuit and large misalignments. Accordingly, the developed wireless charging system continues to transmit power under constant load at up to 25% misalignment. In cases of greater misalignment and open circuit, it shuts itself off.

The primary-side controlled WCS proposed in this paper can be used in e-vehicles with similar power and voltage levels using other compensation topologies that are derivatives of the SS topology.

Author Contributions: Conceptualization, E.Y. and M.B.; methodology, E.Y. and M.B.; software, M.B.; validation, M.B.; formal analysis, E.Y.; investigation, E.Y.; resources, E.Y. and M.B.; data curation, M.B.; writing—original draft preparation, E.Y.; writing—review and editing, E.Y.; visualization, E.Y. and M.B.; supervision, E.Y.; project administration, E.Y.; funding acquisition, M.B. All authors have read and agreed to the published version of the manuscript.

Funding: This research and the APC were funded by [Farba Automotive].

Data Availability Statement: Not applicable.

Conflicts of Interest: The authors declare no conflict of interest.

Abbreviations

Parameters

R_o	equivalent load resistance
R_L	load resistance
M	mutual inductance
$V_o{}'$	input voltage of rectifier in the secondary side of IPT
V_P	Primary side input voltage of IPT
V_F	output voltage of forward converter
L_P, L_S	primary and secondary side self-inductances of IPT
C_P, C_S	primary and secondary side resonance capacitors of IPT
I_P, I_S	primary and secondary side currents of the IPT
ω	operating angular frequency
Q_P, Q_S	primary and secondary side quality factors of IPT
d	distance between the primary and secondary pads of IPT
N_P, N_S	Turn numbers of primary and secondary coils of IPT
f_0	resonance frequency
η	AC-AC efficiency of IPT
$P_o{}'$	input power of the rectifier on the secondary side of IPT
G_{I-V}	current–voltage gain of the IPT
G_{V-V}	voltage–voltage gain of the IPT
η_F	forward converter efficiency
N_F	turn ratio of the forward transformer
D	Duty ratio of the forward converter
L_F, C_F	inductor and capacitor of low-pass filter for forward converter
ω_F	switching frequency of forward converter
ΔI_F, ΔV_F	the ripple in current and voltage of the forward converter output
k	magnetic coupling
V_o, I_o	load voltage and current
V_{F_test}	forward converter test voltage to control IPT load
I_{F_max1}	maximum forward converter current level to set for CC mode
I_{F_max2}	maximum forward converter current level to set for CV mode

Abbreviations

IPT	inductive power transfer
CC	constant current
CV	constant voltage
PTE	power transfer efficiency of IPT
ESR	effective series resistance
PCM	peak current mode
SOC	state of charge
WCS	wireless charging systems

References

1. Gbey, E.; Turkson, R.F.; Lee, S. A Bibliometric Survey of Research Output on Wireless Charging for Electric Vehicles. *World Electr. Veh. J.* **2022**, *13*, 37. [CrossRef]
2. Li, S.; Li, W.; Deng, J.; Nguyen, T.D.; Mi, C.C. A Double-sided LCC compensation network and its tuning method for wireless power transfer. *IEEE Trans. Veh. Technol.* **2015**, *64*, 2261–2273. [CrossRef]
3. Lu, F.; Zhang, H.; Hofmann, H.; Mi, C.C. An inductive and capacitive integrated coupler and its LCL compensation circuit design for wireless power transfer. *IEEE Trans. Ind. Appl.* **2017**, *53*, 4903–4913. [CrossRef]
4. Song, K.; Li, Z.; Jiang, J.; Zhu, C. Constant current/voltage charging operation for series–series and series–parallel compensated wireless power transfer systems employing primary-side controller. *IEEE Trans. Power Electron.* **2018**, *33*, 8065–8080. [CrossRef]
5. Samanta, S.; Rathore, A.K. A New Inductive Power Transfer Topology Using Direct AC–AC Converter with Active Source Current Waveshaping. *IEEE Trans. Power Electron.* **2018**, *33*, 5565–5577. [CrossRef]
6. Vardani, B.; Tummuru, N.R. A Single-Stage Bidirectional Inductive Power Transfer System with Closed-Loop Current Control Strategy. *IEEE Trans. Transp. Electrif.* **2020**, *6*, 948–957. [CrossRef]
7. Huynh, P.S.; Ronanki, D.; Vincent, D.; Williamson, S.S. Overview and Comparative Assessment of Single-Phase Power Converter Topologies of Inductive Wireless Charging Systems. *Energies* **2020**, *13*, 2150. [CrossRef]
8. Wang, Z.; Wei, X.; Dai, H. Design and Control of a 3 kW Wireless Power Transfer System for Electric Vehicles. *Energies* **2016**, *9*, 10. [CrossRef]
9. Hata, K.; Imura, T.; Hori, Y. Maximum efficiency control of wireless power transfer systems with Half Active Rectifier based on primary current measurement. In Proceedings of the IEEE 3rd International Future Energy Electronics Conference and ECCE Asia (IFEEC 2017-ECCE Asia), Kaohsiung, Taiwan, 3–7 June 2017; pp. 1–6.
10. Corti, F.; Reatti, A.; Pierini, M.; Barbieri, R.; Berzi, L.; Nepote, A.; Pierre, P.D.L. A low-cost secondary-side controlled electric vehicle wireless charging system using a full-active rectifier. In Proceedings of the International Conference of Electrical and Electronic Technologies for Automotive, Milan, Italy, 9–11 July 2018; pp. 1–6.
11. Triviño, A.; González, J.M.; Aguado, J.A. Wireless Power Transfer Technologies Applied to Electric Vehicles: A Review. *Energies* **2021**, *14*, 1547. [CrossRef]
12. Miller, M.; Onar, O.C.; Chinthavali, M. Primary-side power flow control of wireless power transfer for electric vehicle charging. *IEEE J. Emerg. Sel. Top. Power Electron.* **2015**, *3*, 147–162. [CrossRef]
13. Zhao, Q.; Wang, A.; Liu, J.; Wang, X. The Load Estimation and Power Tracking Integrated Control Strategy for Dual-Sides Controlled LCC Compensated Wireless Charging System. *IEEE Access* **2019**, *7*, 75749–75761. [CrossRef]
14. Guo, Y.; Zhang, Y. Secondary Side Voltage and Current Estimation of Wireless Power Transfer Systems. *IEEE Trans. Ind. Appl.* **2022**, *58*, 1222–1230. [CrossRef]
15. Liu, Y.; Madawala, U.K.; Mai, R.; He, Z. Primary-Side Parameter Estimation Method for Bidirectional Inductive Power Transfer Systems. *IEEE Trans. Power Electron.* **2021**, *36*, 68–72. [CrossRef]
16. Gati, E.; Kampitsis, G.; Manias, S. Variable frequency controller for inductive power transfer in dynamic conditions. *IEEE Trans. Power Electron.* **2017**, *32*, 1684–1696. [CrossRef]
17. Li, Z.; Song, K.; Jiang, J.; Zhu, C. Constant current charging and maximum efficiency tracking control scheme for supercapacitor wireless charging. *IEEE Trans. Power Electron.* **2018**, *33*, 9088–9100. [CrossRef]
18. Li, Z.; Wei, G.; Dong, S.; Song, K.; Zhu, C. Constant current/voltage charging for the inductor–capacitor–inductor-series compensated wireless power transfer systems using primary-side electrical information. *IET Power Electron.* **2018**, *11*, 2302–2310. [CrossRef]
19. Li, M.; Deng, J.; Chen, D.; Wang, W.; Wang, Z.; Li, Y. A Control Strategy for ZVS Realization in LCC-S Compensated WPT System with Semi Bridgeless Active Rectifier for Wireless EV Charging. In Proceedings of the 2021 IEEE Energy Conversion Congress and Exposition (ECCE), Vancouver, BC, Canada, 10–14 October 2021; pp. 5823–5827.
20. Wang, Y.; Mostafa, A.; Zhang, H.; Mei, Y.; Zhu, C.; Lu, F. Sensitivity Investigation and Mitigation on Power and Efficiency to Resonant Parameters in an LCC Network for Inductive Power Transfer. *IEEE J. Emerg. Sel. Top. Ind. Electron.* **2021**. [CrossRef]
21. Zhang, Y.; Wang, L.; Guo, Y.; Bo, Q.; Liu, Z. An Optimization Method of Dual-side LCC Compensation Networks Simultaneously Considering Output Power and Transmission Efficiency in Two-directions for BWPT Systems. *IEEE J. Emerg. Sel. Top. Ind. Electron.* **2022**. [CrossRef]
22. Bosshard, R.; Badstübner, U.; Kolar, J.W.; Stevanović, I. Comparative evaluation of control methods for Inductive Power Transfer. In Proceedings of the International Conference on Renewable Energy Research and Applications (ICRERA), Nagasaki, Japan, 11–14 November 2012; pp. 1–6.
23. Liu, F.; Lei, W.; Wang, T.; Nie, C.; Wang, Y. A phase-shift soft-switching control strategy for dual active wireless power transfer system. In Proceedings of the IEEE Energy Conversion Congress and Exposition (ECCE), Cincinati, OH, USA, 1–5 October 2017; pp. 2573–2578.
24. Patil, D.; Sirico, M.; Gu, L.; Fahimi, B. Maximum efficiency tracking in wireless power transfer for battery charger: Phase shift and frequency control. In Proceedings of the IEEE Energy Conversion Congress and Exposition (ECCE), Milwaukee, WI, USA, 18–22 September 2016; pp. 1–8.

25. Pellitteri, F.; Campagna, N.; Castiglia, V.; Damiano, A.; Miceli, R. Design, implementation and experimental results of a wireless charger for E-bikes. In Proceedings of the International Conference on Clean Electrical Power (ICCEP), Otranto, Italy, 2–4 July 2019; pp. 364–369.
26. Joseph, P.K.; Elangovan, D.; Arunkumar, G. Linear control of wireless charging for electric bicycles. *Appl. Energy* **2019**, *255*, 113898. [CrossRef]
27. Pellitteri, F.; Boscaino, V.; Di Tommaso, A.O.; Miceli, R. Wireless battery charging: E-bike application. In Proceedings of the International Conference on Renewable Energy Research and Application (ICRERA), Madrid, Spain, 20–23 October 2013; pp. 247–251.
28. Pellitteri, F.; Boscaino, V.; Miceli, R.; Madawala, U.K. Power tracking with maximum efficiency for wireless charging of E-bikes. In Proceedings of the IEEE International Electric Vehicle Conference (IEVC), Florence, Italy, 17–19 December 2014; pp. 1–7.
29. Hou, J.; Chen, Q.; Zhang, L.; Xu, L.; Wong, S.C.; Chi, K.T. Compact Capacitive Compensation for Adjustable Load-Independent Output and Zero-Phase-Angle Input for High Efficiency IPT Systems. *IEEE J. Emerg. Sel. Top. Power Electron.* **2022**. [CrossRef]
30. Cabrera, A.T.; González, J.M.; Aguado, J.A. Design and Implementation of a Cost-Effective Wireless Charger for an Electric Bicycle. *IEEE Access* **2021**, *9*, 85277–85288. [CrossRef]
31. Skorvaga, J.; Frivaldsky, M.; Pavelek, M. Design of a Wireless Charging System for e-Scooter. *Elektron. Ir Elektrotechnika* **2021**, *27*, 40–48. [CrossRef]
32. Stielau, O.H.; Covic, G.A. Design of loosely coupled inductive power transfer systems. In Proceedings of the International Conference on Power System Technology, Perth, WA, Australia, 4–7 December 2000; pp. 85–90.
33. Yildiriz, E.; Kemer, S.B.; Bayraktar, M. IPT design with optimal use of spiral rectangular coils for wireless charging of e-tricycle scooters. *Eng. Sci. Technol. Int. J.* **2022**, *33*, 101082. [CrossRef]
34. Boys, J.T.; Covic, G.A.; Green, A.W. Stability and control of inductively coupled power transfer systems. *Electr. Power Appl.* **2000**, *147*, 37–43. [CrossRef]
35. Sallán, J.; Villa, J.L.; Llombart, A.; Sanz, J.F. Optimal design of ICPT systems applied to electric vehicle battery charge. *IEEE Trans. Ind. Electron.* **2009**, *56*, 2140–2149. [CrossRef]